

Axial Particle Diffusion in Rotating Cylinders

Christian M. Dury and Gerald H. Ristow

Abstract We study the interface dynamics of a binary particle mixture in a rotating cylinder numerically. By considering only the particle motion in axial direction, it is shown that the initial dynamics can be well described by a one-dimensional diffusion process. This allows us to calculate a *macroscopic* diffusion constant and we study its dependence on the inter-particle friction coefficient, the rotation speed of the cylinder and the density ratio of the two components. It is found that radial segregation reduces the drift velocity of the interface. We then perform a *microscopic* calculation of the diffusion coefficient and investigate its dependence on the position along the cylinder axis and the density ratio of the two particle components. The latter dependence can be explained by looking at the different hydrostatic pressures of the two particle components at the interface. We find that the microscopically calculated diffusion coefficient agrees well with the value from the macroscopic definition when taken in the middle of the cylinder.

1 Introduction

A common device used for mixing different kinds of materials is a rotating kiln or cylinder [1] where the mixing rate and the particle dynamics depend on the rotation speed of the cylinder [2,3]. However, when materials which differ in size or density are used, particles with different properties tend to accumulate in different spatial regions which is called *segregation*. Two different types of segregation are commonly observed in rotating cylinders:

- (a) a fast **radial** segregation
- (b) a much slower **axial** segregation.

The latter leads to band formation along the rotational axis and it takes many cylinder rotations before a steady state with respect to the observed band structure is reached [4,5,6,7,8,9,10]. In the case of radial segregation, it usually takes only a few rotations to reach a fully segregated state where the smaller or denser particles form a central core right below the fluidized surface layer. This was

studied experimentally and numerically for varying size ratios [11,12,13,14,15,16] and density ratios [17,18,19]. The amount and direction of segregation depends on the rotation rate [3].

The common method to study the segregation process starts from a well mixed state and records the segregation amount or the spatial pattern as function of time. This works well in the case of *radial* segregation and quantitative results regarding the dependence of the segregation process on rotation speed and size ratio were obtained using a suitable, normalizable order parameter q_∞ [15,16]. However, the *axial* segregation process is much richer due to the three-dimensional particle motion and small changes in the initial mixture seem to have a large effect on the band formation process. The final number of bands, their positions and widths varied from experiment to experiment. For example Nakagawa [7] found that a three band configuration was the most stable after an extended number of rotations. These bands are normally not pure and a radially segregated core of smaller or/and denser particles might still be present [14]. Chicharro et al. [9] rotated two sizes of Ottawa sand for two weeks at 45 revolutions per minute (rpm) and found a final state of two *pure* bands each filling approximately half of the cylinder, i.e. *no* radial core was found.

Depending on the particle kinds used in the experiments, the band formation process is more or less pronounced and for some combinations not observed at all. Different explanations have been proposed:

1. Donald and Roseman [5] concluded from their experiments that no banding occurs when the smaller particles have a smaller *static angle of repose*;
2. das Gupta et al. [6] modified this statement by saying that the relevant quantity is the difference in surface angle of the two components at a specific rotation speed (*dynamic angle of repose*) and
3. Hill and Kakalios [8] proposed a model based on a diffusion equation with an *effective diffusion coefficient* to account for their finding of “reversible axial segregation”.

Recently it was argued that other transport mechanisms can drive the segregation process, especially that avalanches play a role [20].

In order to have a better defined initial configuration for binary mixtures, it was proposed to fill one half of the cylinder with one particle component and the other half with the other component [21] which is sketched in Fig. 1 for a system with particles of different sizes. Such a configuration allows for a detailed analysis of the individual

Received: March 16, 2018/ Revised version: date

Christian M. Dury and Gerald H. Ristow

Fachbereich Physik
 Philipps-Universität
 35032 Marburg, Germany

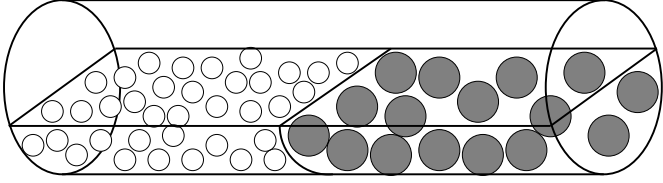


Fig. 1. Sketch of the initial configuration: large particles are all in the right half of the cylinder and shown in gray.

dependencies and will be used as initial state throughout this paper to study the mixing and segregation of binary particle mixtures along the rotational axis numerically.

The paper is organized in the following way: In the next section, we describe our numerical model which solves Newton’s equation of motion for each particle and discuss the physical interpretation of our simulation parameters. In section 3, we demonstrate how different dynamic angles of repose can be obtained using our numerical model and compare their values to experiments. In section 4, the particle dynamics along the rotational axis are described by a one-dimensional diffusion equation and the calculated diffusion constant are studied as function of the inter-particle friction coefficient, the rotation speed of the cylinder and the density ratio of the two components. It is also compared in section 5 to a microscopic calculation of the diffusion coefficient based on the individual particle motion and the agreement is very satisfactory. The conclusions round off the paper.

2

Numerical Model

We use three-dimensional discrete element methods, also known as *granular dynamics* [22], which gives us the advantage to vary particle properties like density and friction coefficient freely, whereas in experiments the number of different kinds of beads is rather limited.

Each particle i is approximated by a sphere with radius R_i . Only contact forces during collisions are considered and the particles are allowed to rotate; we also include rolling resistance to our model to correctly describe the particle rotations (see Ref. [16,23]). The forces acting on particle i during a collision with particle j are

$$F_{ij}^n = -\tilde{Y} (R_i + R_j - \mathbf{r}_{ij} \cdot \hat{n}) - \gamma_n \mathbf{v}_{ij} \cdot \hat{n} \quad (1)$$

in the normal direction (\hat{n}) and

$$F_{ij}^s = -\min(\gamma_s \mathbf{v}_{ij} \cdot \hat{s}(t), \mu |F_{ij}^n|) . \quad (2)$$

in the tangential direction (\hat{s}) of shearing. In Eq. (1) γ_n represent the dynamic damping coefficient and Eq. (2) γ_s represent the dynamic friction force in the tangential direction. \mathbf{r}_{ij} represents the vector joining both centers of mass, \mathbf{v}_{ij} represents the relative motion of the two particles, and \tilde{Y} is related to the Young Modulus of the investigated material. Dynamic friction for particle–particle collisions is defined in this model to be proportional to the relative velocity of the particles in the tangential direction which is a good approximation in many cases [24].

During particle–wall contacts, the wall is treated as a particle with infinite mass and radius. In the normal direction, Eq. (1) is applied, whereas in the tangential direction, the static friction force

$$\tilde{F}_{ij}^s = -\min(k_s \int \mathbf{v}_{ij} \cdot \hat{s}(t) dt, \mu |F_{ij}^n|) \quad (3)$$

is used. This is motivated by the observation that when particles flow along the free surface, they dissipate most of their energy in collisions and can come to rest in voids left by other particles. This is not possible at the cylinder walls. In order to avoid additional artificial particles at the walls we rather use a static friction law to avoid slipping and allowing for a static surface angle when the rotation is stopped. Both tangential forces are limited by the Coulomb criterion, see Eqs. (2) and (3), which states that the magnitude of the tangential force cannot exceed the magnitude of the normal force multiplied by the friction coefficient μ . The coefficient of restitution for particle–particle collisions is set to 0.58 and to 0.76 for particle–wall collisions. The large particles have a diameter of 3 mm and a density of $\rho_l = 1.3 \frac{g}{cm^3}$. The material properties of the large particles were chosen to correspond to the measured values of mustard seeds [25]. The small particles have a diameter of 2 mm. In order to save computer time, we set \tilde{Y} to $8 \cdot 10^3$ Pa m which is about one order of magnitude softer than desired, but we checked that this has no effect on the investigated properties of the material. This gives a contact time during collisions of $8.5 \cdot 10^{-5}$ s. The total number of particles we used were up to 13 300.

3

Dynamic Angle of Repose

Using numerical simulations enables us to study arbitrary angle differences by varying the inter-particle friction coefficient μ in Eqs. (2) and (3). For collisions between large particles, a value of $\mu_l = 0.2$ is used which gives a dynamic angle of repose similar to the measured values of mustard seeds [26]. When large particles touch the wall, a value of $\mu_w = 0.4$ is used to avoid slipping at the boundary. The additional friction at the end caps leads to an angle difference of 5° in our case which is in agreement with experiments [26]. In order to test different angle differences, the inter-particle friction coefficient for the small particles, μ , was varied from 0.05 to 0.4. For collisions between large and small particles, a value of $\mu_{\text{eff}} = \sqrt{\mu_l \mu}$ is used.

In Fig. 2, we show the spatial variation of the dynamic angle of repose, Θ , and its dependence on μ . The cylinder length was 7 cm and the region initially occupied by small particles corresponds to the interval $z = 0 \dots 3.5$ cm to the right. The angles were measured by dividing the cylinder into 22 slices along the rotational axis and we determined the angle of repose for a rotation speed of 15 rpm via the center of mass of all particles in each slice. In order to reduce the fluctuations, we averaged the angles over an interval of 2 seconds after the first initial avalanches. When μ is increased from 0.05 to 0.4, the measured angle at the right wall shows a drastic increase from roughly 10° to 45° . For glass beads it was found that the dynamic angle of repose does hardly depend on the particle size [27]

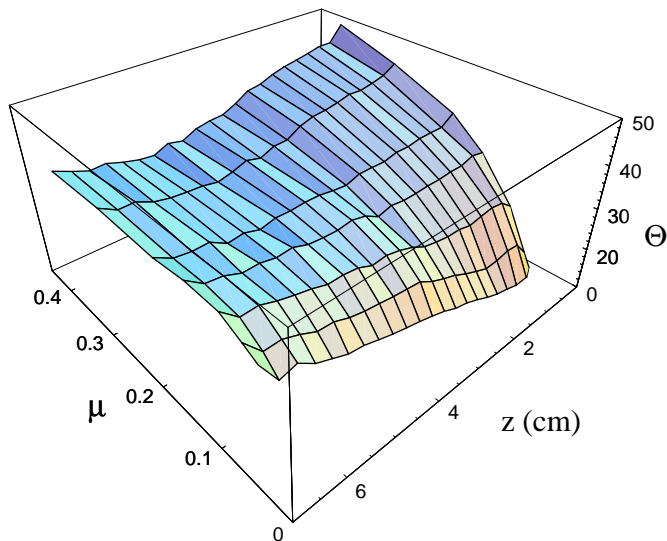


Fig. 2. Surface plot showing the dynamic angle of repose as function of friction parameter μ and position along the rotational axis z .

and we achieve the same effect by using a value of $\mu = 0.2$ in our numerical model. Also clearly visible are the effects of the two cylinder end caps at $z = 0$ and 7 cm, which lead to a higher angle due to the additional wall friction and was studied in detail in Ref. [26].

From our numerical data, we can also calculate the concentration dependence of the dynamic angle of repose. In order to reduce the influence of the boundary caps, we only use the values for the angle of repose from the 16 central slices of the total 22 slices and calculate the volumetric concentration of small particles in each slice, denoted by C , which is shown in Fig. 3 as function of the friction coefficient of the small particles, μ . The graph shows the same general trend as Fig. 2 and one can read off that no concentration dependence is observed for $\mu = 0.2$ which agrees very well with an experimental study of 2 and 4 mm liquid-filled spheres [28]. In the same experiment, the concentration dependence was investigated for a rotation speed of 30 rpm and it was found that the angle increases with increasing concentration. Our numerical data clearly indicates that the same concentration dependence can be found in our case when the small particles have a higher friction coefficient than the large particles, see e.g. the values for $\mu = 0.4$ in Fig. 3.

4 Mixing at the Interface

The shape dynamics and the interface propagation of a binary particle mixture was investigated for 1 and 4 mm liquid-filled spheres using magnetic resonance imaging (MRI) [29]. The initial sharp interface between the regions occupied by large and small particles, see Fig. 1, will deform and move mostly due to particle diffusion in the fluidized surface layer. A nearly fully segregated core of small particles was observed after rotating a 10 cm long, 7 cm wide cylinder for 10 min at 11.4 rpm. Since recording a full three-dimensional MRI-image is still a time-consuming

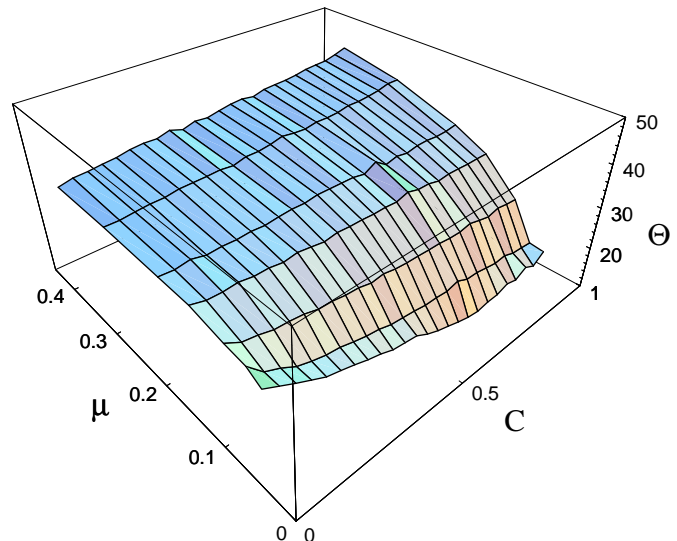


Fig. 3. Surface plot showing the dynamic angle of repose as function of friction parameter μ and concentration of small particles C .

task and requires special equipment, most studies divide the cylinder into vertical slices along the rotational axis and record the particle concentration in each slice [30,31,21]. This leads to a one-dimensional description of the mixing or segregation process and a typical example from our numerical study is shown in Fig. 4. The origin was shifted by half the cylinder length to give a position of $z = 0$ cm for the initial interface which will be used throughout the rest of this chapter. The friction coefficient was $\mu = 0.2$ and the density ratio $\rho/\rho_l = 0.82$ where ρ_l denotes the reference density of the large particles. The initial sharp interface is clearly visible to the left and one notes how the interface broadens in time. For $t = 36$ s, the first small particles have reached the right wall and consequently, the concentration values at the boundaries will start to deviate from their initial values, already visible in the profile to the far right for $t = 50$ s.

4.1 Approximation through pure Diffusion Process

Assuming random particle motion in the axial direction (z axis), one component systems could be well described by a diffusion process according to Fick's Second Law [30,31]. The interface of a two component system can also be studied in this fashion and the diffusion equation reads

$$\frac{\partial C(z, t)}{\partial t} = \frac{\partial}{\partial z} \left(D \frac{\partial C(z, t)}{\partial z} \right) \quad (4)$$

where $C(z, t)$ and D denote the relative concentration by volume of the smaller particles and the corresponding diffusion coefficient, respectively. The initial condition for a cylinder with length L are

$$C(z, 0) = \begin{cases} 1, & -\frac{L}{2} \leq z < 0 \\ 0, & 0 < z \leq \frac{L}{2} \end{cases}$$

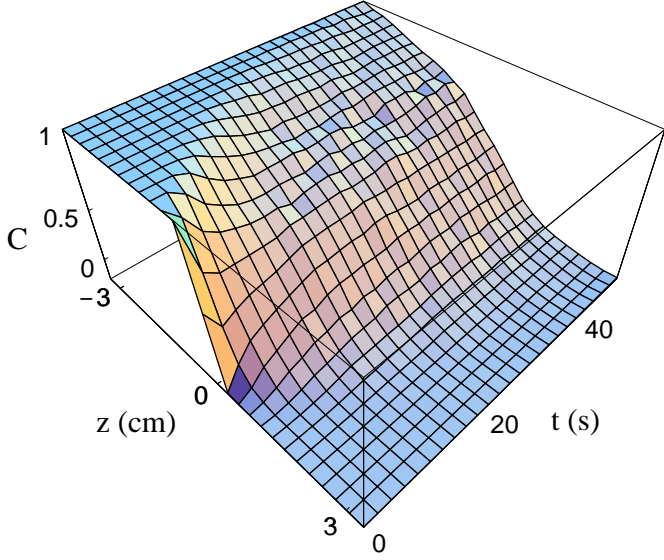


Fig. 4. Surface plot showing the time evolution of the concentration profile for small particles along the rotational axis z .

whereas the boundary conditions read

$$\left. \frac{\partial C}{\partial z} \right|_{z=-\frac{L}{2}} = \left. \frac{\partial C}{\partial z} \right|_{z=\frac{L}{2}} = 0$$

which states, that there is zero axial flux at the boundaries due to the end caps.

For a constant diffusion coefficient, Eq. (4) can be solved analytically for the specified initial and boundary conditions and the solution reads

$$C(z, t) = \frac{1}{2} - \frac{2}{\pi} \sum_{k=1}^{\infty} \frac{1}{2k-1} \exp\left(-\frac{(2k-1)^2 \pi^2 Dt}{L^2}\right) \times \sin\left(\frac{(2k-1)\pi z}{L}\right). \quad (5)$$

In order to study the short time behaviour, we can solve our system by diffusion in an infinite cylinder. This is valid as long as the concentrations at the real cylinder boundaries have their initial values. Solving Eq. (4) for this system gives [32]

$$C(z, t) = \frac{1}{2} \left[1 - \operatorname{Erf}\left(\frac{z}{2\sqrt{Dt}}\right) \right] \quad (6)$$

where $\operatorname{Erf}(x) = \frac{2}{\sqrt{\pi}} \int_0^x e^{-t^2} dt$ is the error function. To determine now the diffusion coefficient we build the norm of

$$\mathfrak{A}(t) := (C(\cdot, t) - C(\cdot, \infty)) \in \mathbf{L}_2[0, \frac{L}{2}] \quad (7)$$

where $C(z, \infty) = \frac{1}{2}$ is the steady state concentration:

$$\begin{aligned} \|\mathfrak{A}(t)\|^2 &= \int_{-L/2}^0 (C(z, t) - C(z, \infty))^2 dz \\ &= \int_{-L/2}^0 \left(\operatorname{Erf}\left(\frac{z}{2\sqrt{Dt}}\right) \right)^2 dz \end{aligned} \quad (8)$$

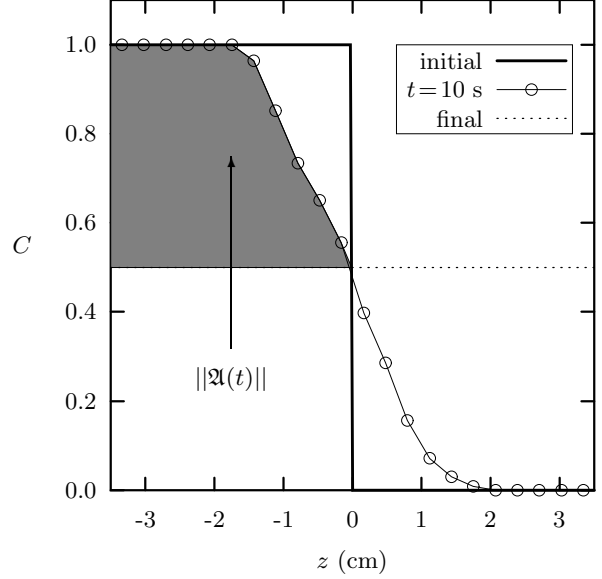


Fig. 5. Concentration profiles for different t times, from Fig 4.

which leads to

$$\begin{aligned} &= \frac{L}{2} \operatorname{Erf}^2\left(\frac{L}{4\sqrt{Dt}}\right) - \sqrt{\frac{Dt}{\pi}} \left\{ -2\sqrt{2} \operatorname{Erf}\left(\frac{L}{2\sqrt{2Dt}}\right) \right. \\ &\quad \left. + 4 \exp\left(\frac{-L^2}{16Dt}\right) \operatorname{Erf}\left(\frac{L}{4\sqrt{Dt}}\right) \right\}. \end{aligned} \quad (9)$$

But this result holds anyway just for small t where $C(L/2, t) \simeq 1$ and therefore we have

$$\operatorname{Erf}\left(\frac{L}{4\sqrt{Dt}}\right) \simeq 1$$

and out of the monotonic behavior of $\operatorname{Erf}()$ also

$$\operatorname{Erf}\left(\frac{L}{2\sqrt{2Dt}}\right) \simeq 1$$

and for small t we also have

$$\exp\left(-\frac{L^2}{16Dt}\right) \simeq 0.$$

Using this we finally get

$$\|\mathfrak{A}(t)\| = \|\mathfrak{A}(0)\| \left(1 - \frac{4}{L} \sqrt{\frac{2Dt}{\pi}} \right). \quad (10)$$

The physical interpretation of $\|\mathfrak{A}(t)\|$ will become clearer by looking at a concentration profile extracted from Fig. 4 which is shown in Fig. 5. Three profiles are shown, namely the theoretical initial concentration profile as thick line, a computed profile for $t = 10$ s denoted by circles and the expected steady state profile as dotted line. The quantity $\|\mathfrak{A}(t)\|$ is a measure of how close the concentration profile

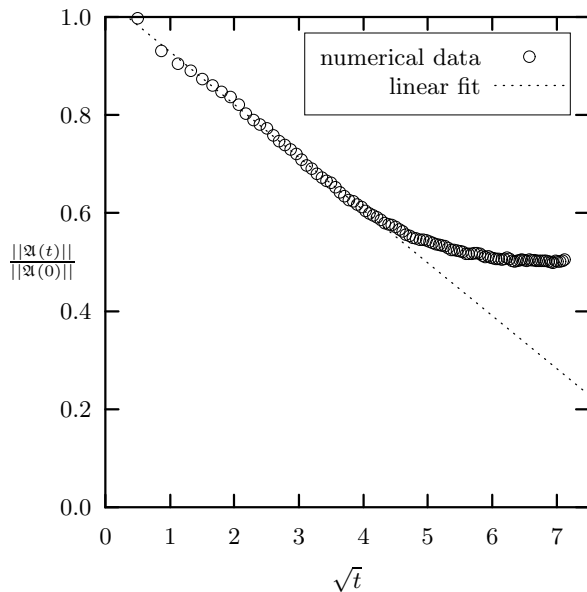


Fig. 6. Plot of $\frac{\|\mathfrak{a}(t)\|}{\|\mathfrak{a}(0)\|}$ vs. \sqrt{t} . The linear fit, shown as dashed line, is used to determine the diffusion coefficient.

is to the expected steady state profile and we shaded the region which enters our calculations in Eq. (8).

The highest value of $\|\mathfrak{a}(t)\|$ is given for $t = 0$ s and a decrease linear in \sqrt{t} is expected for short times, see Eq. (10). This is shown in Fig. 6, using the same simulation parameters as for Figs. 4 and 5, where we plot $\|\mathfrak{a}(t)\|$ normalized by the initial value $\|\mathfrak{a}(0)\|$ vs. \sqrt{t} . From the slope of the linear fit shown as dotted line in Fig. 6, we can calculate a constant diffusion coefficient based on our approximations which gives $D = 0.022 \pm 0.002$ cm²/s and agrees well with values extracted from experiments [29]. When small particles are close to the opposite wall, our approximation of an infinite long cylinder does not hold anymore which leads to a systematic deviation from the \sqrt{t} -behaviour, visible for times larger than 20 s in Fig. 6. For this specific run, the first small particle can be found in the slice at the opposite wall at $t = 32$ s. This time difference of 15 s where the graph deviates from the linear behaviour and the time the first particle reaches the boundary comes from the fact that the particles feel the boundary quite early.

4.2 Dependence on Friction Coefficient

The dependence of the diffusion coefficient on the friction coefficient of the small particles is quite small and shown in Fig. 7. The tendency of lower D for higher μ even persists for quite large friction coefficient, where small particles have a much higher angle of repose than the large particles (for $\mu = 0.2$ and $\Omega = 15$ rpm the angle of repose is the same for large and small particles). This weak dependence can be explained by the so called “roller coaster” effect. Suppose we have a sharp front between small and large particles, then the angle of repose exhibits also a sharp front. A particle on top of the free surface with the higher

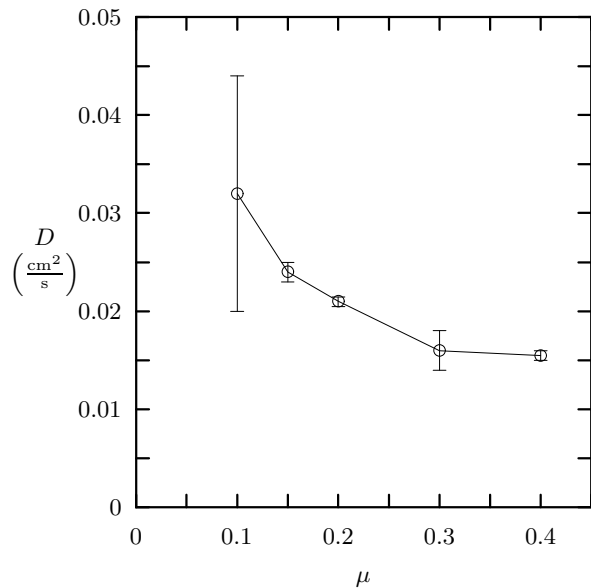


Fig. 7. Diffusion coefficient for different values of μ of the small particles.

angle of repose will see the angle difference and the motion of the particle will be directed towards the region of the lower angle of repose. But the same thing happens in the lower part of the free surface, where now the situation is reversed, and the particle will move back. Therefore, in first approximation, there will be no net effect on the drift (or diffusion) due to this difference in the angle of repose, and what is left is a normal random walk on the free surface of the particle in the direction along the rotational axis. If we now pay tribute to the fact, that our particles have different sizes and therefore will exhibit radial segregation, the “roller coaster” motion will not be as perfect as described above. Suppose the small particles exhibit a higher angle of repose ($\mu > 0.2$), the path of small particles will lead over the free surface of the large particles and they can therefore be trapped into a radial core, thus will be removed from the free surface motion and so also from the diffusion process, which decreases the diffusion coefficient D . On the other hand for $\mu < 0.2$, large particle will not be trapped into a core and can continue to participate in the diffusional process even when they get stuck during the “roller coaster” motion, which is more probable the wider the “roller coaster” path, i.e. the larger the difference in the angle of repose. So D increases with decreasing μ .

In order to demonstrate the increase of radial segregation due to an increase of friction coefficient, we show in Fig. 8 two cross sections of the cylinder which represent the configuration close to the initial interface. For a value of $\mu = 0.15$, we show in part (a) the particle configuration at $t = 33$ s and a segregation of the small particles, drawn in white, is hardly visible. In contrast to this, a nice segregation is visible in part (b), which shows a configuration for $\mu = 0.4$ and $t = 27$ s. This supports our hypothesis that radial segregation will *hinder* the diffusion of small particles and thus decrease the diffusion coefficient with increasing friction coefficient.

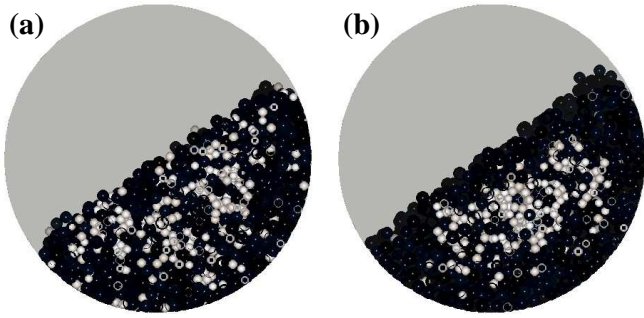


Fig. 8. Cross section of the cylinder close to the initial interface for (a) $\mu = 0.15$ at $t = 33$ s and (b) $\mu = 0.4$ at $t = 27$ s. Large particles are shown in black and small particles in white.

4.3 Dependence on Rotation Speed

When investigating the mixing process of glass beads, Hogg et al. [30] found that the dynamics could be well described by using the number of revolutions instead of the time in Eq. (4). This directly implies that the calculated diffusion constant should be directly proportional to the rotation speed of the cylinder. We checked this for our system by investigating an Ω -range of 7.5 to 45 rpm for the simulation parameters $\rho/\rho_l = 1$ and $\mu = 0.15$ which is shown in Fig. 9. Also shown as dashed line is the linear dependence proposed in [30] and as expected it is only a valid assumption for low rotation speeds. On the other hand, our numerically calculated values for D rather show a more than linear dependence when the whole Ω -range is considered, which was fitted by a quadratic function and added as a solid line to Fig. 9. This deviation from the linear behavior is due to the fact that the particles will bounce off the cylinder wall, after they flowed down the free surface. This effect of bouncing is also observed in experiments [3].

4.4 Dependence on Density Ratio

The particle motion depends on the density ratio ρ/ρ_l which is illustrated in Fig. 10 for a constant value of $\mu = 0.2$. To the left, Fig. 10a, the diffusion constant is plotted as function of this density ratio showing a minimum value for $\rho/\rho_l = 1$ and a large increase for lower and higher values. In contrast to the previous section, radial segregation will be present towards both sides of the graph. In general, smaller and denser particles will segregate radially, so increasing the density ratio will enhance radial segregation, but when decreasing the density ratio, the larger particles become denser and eventually the large particles will segregate into the radial core. Also shown in the same graph as inset is a magnification of the region close to $\frac{\rho}{\rho_l} = 1$ with a non-linear fit as solid line. This inset shows that our numerical model always gives a diffusion coefficient larger than zero thus indicating that the front is *not* stable, regardless of the density ratio of the two particle components.

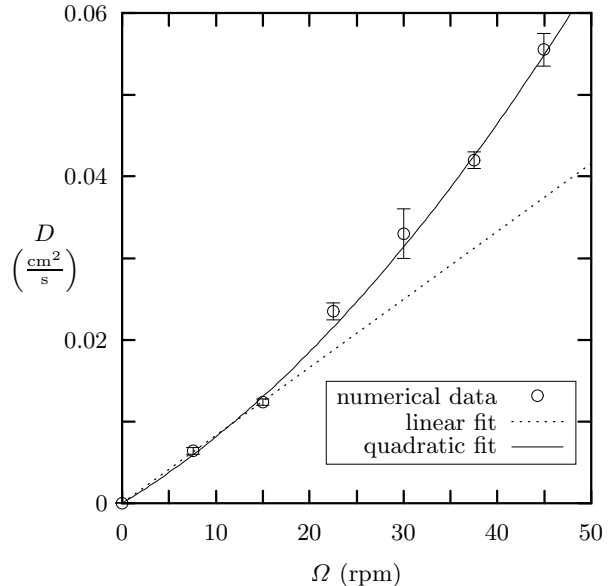


Fig. 9. Diffusion coefficient for different values of the angular velocity Ω of the cylinder.

In order to quantify this process, we use a procedure outlined in Refs. [15,16] to normalize the final amount of segregation. The drum is divided into concentric rings and the final percentage by volume of small particles for large times is estimated in each ring and normalized with respect to a perfectly well radially segregated configuration. Due to the non-negligible width of the fluidized layer, a value of one cannot be achieved. This quantity, denoted by q_∞ , is plotted in Fig. 10b as function of the density ratio. With increasing density ratio, q_∞ increases and saturates around a value of 0.6. The slight decrease for values of $\rho/\rho_l > 2$ is due to the definition of q_∞ which does not take the shifting of the center of mass of the smaller particles into account. For $\rho/\rho_l = 0.5$, the two competing effects of size- and mass-segregation cancel each other and we get a perfect mixing of small and large particles indicated by a small value of q_∞ in Fig. 10b.

Remembering our hypothesis that radial segregation will hinder diffusion from Sec. 4.2, one might wonder why the diffusion coefficient starts to rise again for $\rho/\rho_l > 1$ where we get better segregation, whereas for $\rho/\rho_l < 1$ the diffusion coefficient rises as expected. In contrast to the previous section, we now have to take different densities for the particles into account. We are starting with an initial front where the small particles are on the left and the large particles on the right half of the cylinder (see Fig. 1). The pressure at the interface resulting from the particles above is in first approximation the hydrostatic pressure for granular media [33]:

$$p = c\rho g \left(1 - e^{-\frac{h_d}{c}}\right) \quad (11)$$

where c is a parameter, which depends on the friction coefficient and the boundaries of the investigated geometry. The initial pressure for small depths h_d is like in a fluid $p = \rho g h_d$, but for larger h_d the pressure saturates exponentially to $p = \rho g c$, in contrast to all normal liquids.

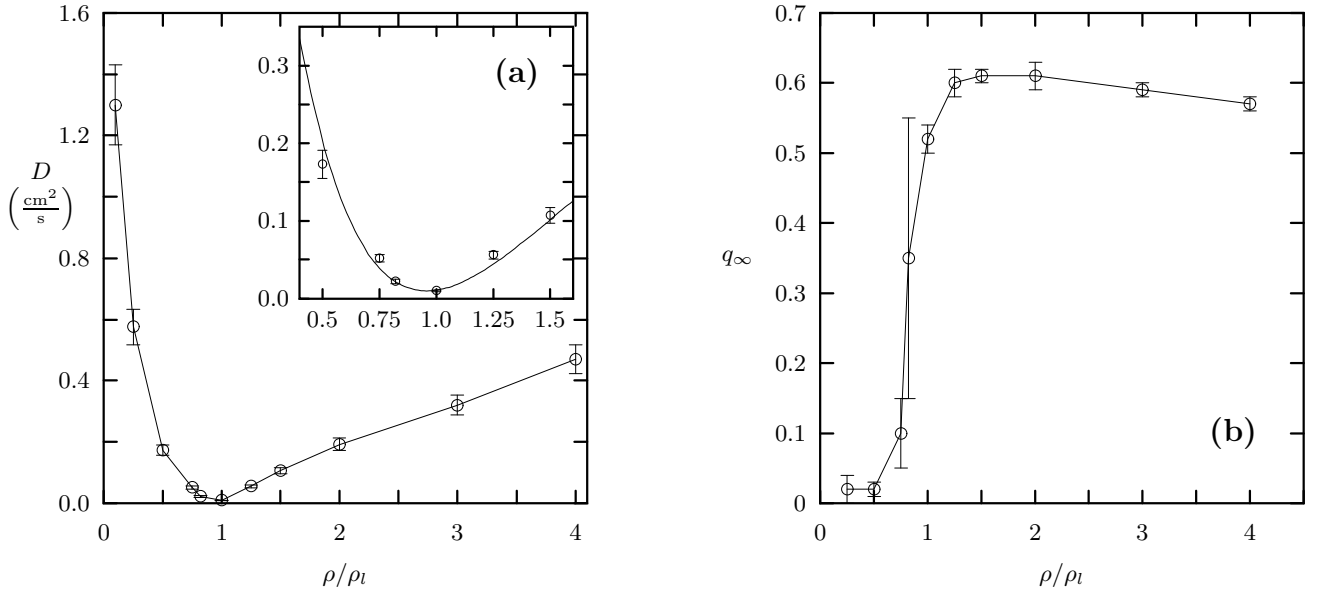


Fig. 10. Calculation of the functional dependence on the density ratio $\frac{\rho}{\rho_l}$ of the small particles for (a) diffusion coefficient, D , where the inset magnifies the region close to $\frac{\rho}{\rho_l} = 1$ with a non-linear fit as solid line and (b) final amount of segregation, q_∞ .

This general pressure dependence is by itself an interesting property for granular media and is independent of the grain size.

For density ratios different than 1, we get a pressure difference at the interface which enhances the mixing of the particles. This results in our simple model in a higher diffusion coefficient and consequently, we get a minimum in D for $\rho/\rho_l = 1$ which is clearly visible in Fig. 10a. This phenomena will be discussed in more detail in section 5.2 below.

5 Microscopic Calculation of Diffusion Coefficient

Another way to investigate the front diffusion is by looking at the particle trajectories directly. When recording only the displacement of the particles along the rotational axis, we obtain a *microscopic* definition of a diffusion coefficient, D_m , through

$$\langle z(t)^2 \rangle - \langle z(0) \rangle^2 = 2D_m t + \langle z(0) \rangle^2, \quad (12)$$

where the spatial average is done over all N investigated particles via

$$\langle z(t) \rangle := \frac{1}{N} \sum_{i=1}^N z_i(t). \quad (13)$$

This technique to obtain a microscopic diffusion constant is similar to the one used in the experiments by Zik and Stavans [34] who investigated the diffusional behaviour of vertically shaken granular material. It enables us to explicitly consider a drift of the particles whereas this was incorporated into the macroscopic diffusion constant presented in the previous section. The drift velocity, v , is defined by the following relation:

$$\langle z(t) \rangle - \langle z(0) \rangle = vt. \quad (14)$$

Another possibility to obtain a microscopic diffusion coefficient would be

$$\langle (z(t) - z(0))^2 \rangle = 2D'_m t,$$

but in this case, one would also absorb a possible drift into the diffusion coefficient. It is therefore only useful for pure diffusion processes and thus will not be used further in this section, because we want to investigate the drift velocity and the diffusion coefficient separately.

5.1 Diffusion Coefficient

The initial particle rearrangement when the cylinder starts to rotate cannot be described by a diffusion process. Therefore, we begin all our measurements at the point when the continuous flow has set in which corresponds to one eighth of a cylinder revolution. In order to resolve the diffusion process spatially, we divide the cylinder into 14 equal slices along the rotational axis and calculate the microscopic diffusion coefficient in each slice from the particle trajectories that start in the corresponding slice. This is done for different density ratios, ρ/ρ_l , of a binary particle mixture and shown in Fig. 11a. Changing the density ratio has a dramatic effect on the diffusion coefficient, increasing the maximum of D_m by a factor of ten when the density of the smaller particles is increased by a factor of 4. In the case where $\rho/\rho_l > 1$, the maximum diffusion coefficient can be found in the region of the larger particles ($z > 0$ cm) and for $\rho/\rho_l < 1$ in the region of the smaller particles; i.e. the spatial maximum of D_m lies on the side of the lighter particles for all density ratios. Nevertheless, in each case the maximum value of the diffusion coefficient is close to the middle.

For comparison, we also calculated the diffusion coefficient for a system with only the larger particle component

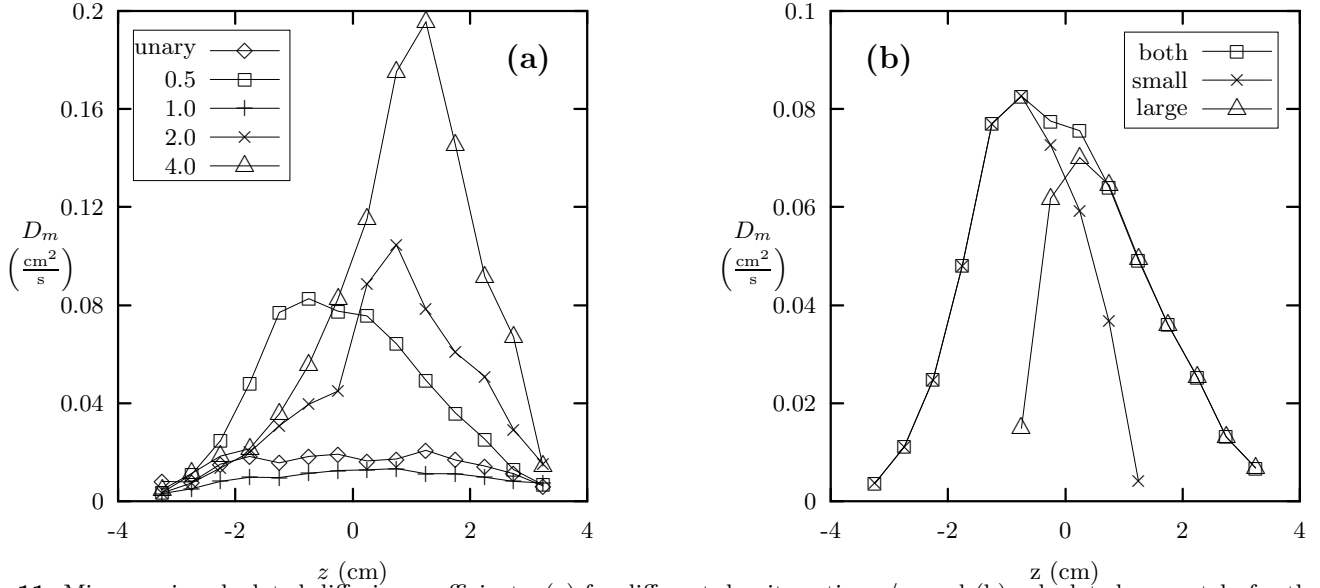


Fig. 11. Microscopic calculated diffusion coefficients: (a) for different density ratios ρ/ρ_l and (b) calculated separately for the small and large particles for $\rho/\rho_l = 0.5$.

which is referred to as *unary* mixture. One thing to note is that the diffusion coefficients for the binary mixture with equal density, denoted by a cross (+) and the unary mixture, denoted by a diamond (\diamond) in the following plots, nearly agree despite the size difference in the binary mixture and hardly show a spatial variation.

In Fig. 11b, we calculate D_m separately for the smaller and larger particles using a density ratio of $\rho/\rho_l = 0.5$. The squares (\square) denote the average diffusion coefficient, as already shown in Fig. 11a and the crosses (\times) and triangles (\triangle) stand for the diffusion coefficient of the smaller and larger particles, respectively. In this case, the maximum of D_m for the smaller particles is larger than for the larger particles. It is also seen that the maximum diffusion coefficient for the smaller particles lies in the region where the small particles have been initially. For the larger particles, the maximum value of the diffusion coefficient lies in the region where the larger particles have been initially and both maxima are very close to the initial interface.

The difference in the maximum value of the diffusion coefficient of the larger and the smaller particles, ΔD_m , is shown in Fig. 12 as function of the density ratio. For a value of $\rho/\rho_l \gtrsim 1$, the larger particles have a larger maximum diffusion coefficient which agrees with the experimental observation that for particles with the same density the large particles have a higher mobility than the smaller particles [6]. For values $\rho/\rho_l < 1$, the mobility of the smaller particles is higher, resulting in a negative difference in Fig. 12. The linear least-square fit using all data points is shown as solid line.

5.2 Drift Velocity

By using the definition given in Eq. (14), we can calculate in each of the 14 slices an average drift velocity of all particles. This is plotted in Fig. 13a for different density ratios ρ/ρ_l . For comparison, the spatial dependence for a unary

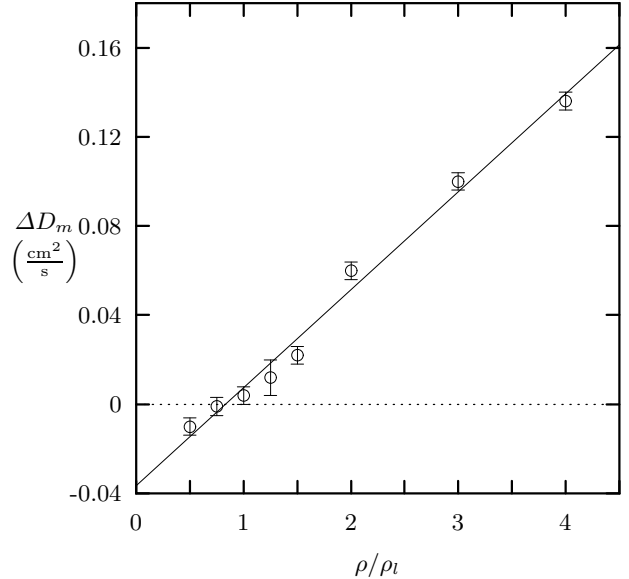


Fig. 12. Difference in the maximum value of the diffusion coefficient of the larger and smaller particles as function of density ratio. The linear least-square fit is shown as solid line.

mixture is also shown, (\diamond), and as before is very close to the dependence of an equal density binary mixture, (+). A much larger drift velocity with a well pronounced maximum at $z < 0$ and minimum at $z > 0$ is observed for $\rho/\rho_l \neq 1$, showing that the global motion exchanges particles across the interface. The larger the density ratio, the larger the region with a positive drift velocity. Consequently, the position corresponding to $v = 0$ will move to the right for *increasing* density ratios and move to the left for *decreasing* density ratios. Please note that this description only applies to the situation shortly after the start of the rotation since a symmetric profile is expected in the

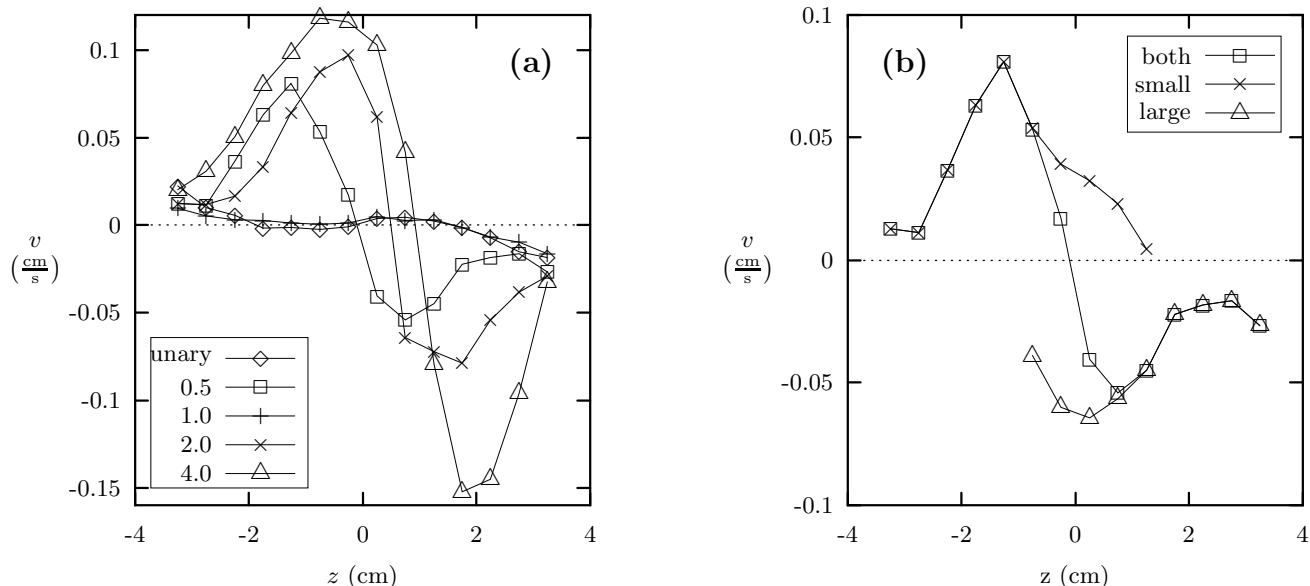


Fig. 13. Microscopic calculated drift velocities: (a) for different density ratios ρ/ρ_l and (b) calculated separately for the small and large particles for $\rho/\rho_l = 0.5$.

steady state due to the symmetry of the problem. The drift velocity can be explained by applying a “hydrostatic picture” again: The hydrostatic pressure at the interface is given by Eq.(11). If we now have two different values for ρ at the interface, there will be a pressure difference of

$$\Delta p \propto |\rho - \rho_l|g \left(1 - e^{-\frac{h_d}{c}}\right) \quad (15)$$

which causes the drift. This drift will not happen on the free surface (where the pressure difference is zero), instead the denser particle will push their way through the lighter ones near the center of revolution, which is well below the rotational axis. Even though the “roller coaster” effect still applies here due to the motion inside the granular material (see section 4.2 for more details), we get a drift in the case of two different densities for the particles.

In Fig. 13b, the individual drift velocities for the smaller and larger particles are shown along the rotational axis. The density ratio was $\rho/\rho_l = 0.5$ and one observes that the particles close to the end caps of the cylinder hardly drift at all. On the other hand, the drift velocity is very large for both components in regions close to the initial interface. Since the initial stage of the interface dynamics was investigated, the drift velocity is positive everywhere for the smaller particles and negative everywhere for the larger particles which clearly shows the particle exchange over the initial interface.

6 Conclusions

We started with an initially sharp front of particles with different properties and looked how this front gets diffused. In the first part of this paper we showed that this process can be well approximated by a pure diffusional process, which was originally applied only to the case of one particle component. Also we found that radial segregation hinders diffusion, because the process of radial

segregation will sort the smaller particles out which are then unable to take place in the diffusion process.

When changing the density of the small particles, we get least mixing for particles with the same density. For different density there is a pressure difference at the interface and the denser particles will penetrate into the lighter ones. This is not a pure diffusional process anymore, because of the non-vanishing drift of the particles, it is more like a core movement combined with diffusion.

Previous to this work the core was mostly thought to be a solid block in which no (or just minimal) movements can take place. We now showed that for different particle densities, and maybe also for differences in other particle properties, core movement is indeed possible. This could shed light on future work on the axial segregation mechanism.

Acknowledgments

We would like to thank the HLRZ in Jülich and the HRZ Marburg for supporting us with a generous grant of computer time on their Cray T3E and IBM SP2, respectively. Financial support by the Deutsche Forschungsgemeinschaft is also gratefully acknowledged.

References

1. J. Bridgewater, “Fundamental Powder Mixing Mechanisms,” *Powder Technol.* **15**, 215 (1976).
2. H. E. Rose, “A Suggested Equation Relating to the Mixing of Powders and its Application to the Study of the Performance of Certain Types of Machine,” *Trans. Instn Chem. Engrs.* **37**, 47 (1959).
3. N. Nityanand, B. Manley, and H. Henein, “An Analysis of Radial Segregation for Different Sized Spherical Solids in Rotary Cylinders,” *Metall. Trans. B* **17**, 247 (1986).

4. Y. Oyama, "(in Japanese)," *Bull. Inst. Phys. Chem. Res. (Tokyo)*, Rep. **18**, 600 (1939).
5. M. B. Donald and B. Roseman, "Mixing and Demixing of Solid Particles," *Br. Chemical Engineering* **7**, 749 (1962).
6. S. Das Gupta, D. V. Khakhar, and S. K. Bathia, "Axial Segregation of Particles in a Horizontal Rotating Cylinder," *Chem. Engineering Science* **46**, 1513 (1991).
7. M. Nakagawa, "Axial Segregation of Granular Flows in a Horizontal Rotating Cylinder," *Chem. Engineering Science-Shorter Communications* **49**, 2544 (1994).
8. K. M. Hill and J. Kakalios, "Reversible Axial Segregation of Rotating Granular Media," *Phys. Rev. E* **52**, 4393 (1995).
9. R. Chicharro, R. Peralta-Fabi, and R. M. Velasco, "Segregation in Dry Granular Systems," In *Powders & Grains 97*, R. P. Behringer and J. T. Jenkins, eds., p. 479 (Balkema, Rotterdam, 1997).
10. K. Choo, T. C. A. Molteno, and S. W. Morris, "Traveling Granular Segregation Patterns in a Long Drum Mixer," *Phys. Rev. Lett.* **79**, 2975 (1997).
11. E. Clément, J. Rajchenbach, and J. Duran, "Mixing of a Granular Material in a Bidimensional Rotating Drum," *Europhys. Lett.* **30**, 7 (1995).
12. F. Cantelaube and D. Bideau, "Radial Segregation in a 2D Drum: an Experimental Analysis," *Europhys. Lett.* **30**, 133 (1995).
13. G. Baumann, I. M. Janosi, and D. E. Wolf, "Surface Properties and Flow of Granular Material in a Two-Dimensional Rotating Drum Model," *Phys. Rev. E* **51**, 1879 (1995).
14. K. M. Hill, A. Caprihan, and J. Kakalios, "Bulk Segregation in Rotated Granular Material Measured by Magnetic Resonance Imaging," *Phys. Rev. Lett.* **78**, 50 (1997).
15. C. M. Dury and G. H. Ristow, "Radial Segregation in a Two-Dimensional Rotating Drum," *J. Phys. I France* **7**, 737 (1997).
16. C. M. Dury and G. H. Ristow, "Competition of Mixing and Segregation in Rotating Cylinders," submitted to *Phys. Fluids*, 1998.
17. G. H. Ristow, "Particle Mass Segregation in a Two-Dimensional Rotating Drum," *Europhys. Lett.* **28**, 97 (1994).
18. G. Metcalfe and M. Shattuck, "Pattern Formation during Mixing and Segregation of Flowing Granular Materials," *Physica A* **233**, 709 (1996).
19. D. V. Khakhar, J. J. McCarthy, and J. M. Ottino, "Radial Segregation of Granular Mixtures in Rotating Cylinder," *Phys. Fluids* **9**, 3600 (1997).
20. V. Frette and J. Stavans, "Avalanche-mediated Transport in a Rotating Mixture," *Phys. Rev. E* **56**, 6981 (1997).
21. M. Nakagawa, J. L. Moss, K. Nishimura, and T. Ozeki, "Stable Configuration of Binary Mixtures in a Horizontal Rotating Cylinder: Axial Migration of Granular Particles," In *Powders & Grains 97*, R. P. Behringer and J. T. Jenkins, eds., p. 495 (Balkema, Rotterdam, 1997).
22. G. H. Ristow, "Granular Dynamics: a Review about recent Molecular Dynamics Simulations of Granular Materials," In *Annual Reviews of Computational Physics I*, D. Stauffer, ed., p. 275 (World Scientific, Singapore, 1994).
23. C. M. Dury, Ph.D. thesis, University of Marburg, Marburg, Germany, 1998.
24. J. Schäfer, S. Dippel, and D. E. Wolf, "Force Schemes in Simulations of Granular Materials," *J. Phys. I France* **6**, 5 (1996).
25. M. Nakagawa, S. Altobelli, A. Caprihan, E. Fukushima, and E.-K. Jeong, "Non-invasive Measurements of Granular Flows by Magnetic Resonance Imaging," *Experiments in Fluids* **16**, 54 (1993).
26. C. M. Dury, G. H. Ristow, J. L. Moss, and M. Nakagawa, "Boundary Effects on the Angle of Repose in Rotating Cylinders," *Phys. Rev. E* **57**, 4491 (1998).
27. O. Zik, D. Levine, S. G. Lipson, S. Shtrikman, and J. Stavans, "Rotationally Induced Segregation of Granular Materials," *Phys. Rev. Lett.* **73**, 644 (1994).
28. K. M. Hill, J. Kakalios, K. Yamane, Y. Tsuji, and A. Caprihan, "Dynamic Angle of Repose as a Function of Mixture Concentration: Results from MRI Experiments and DEM Simulations," In *Powders & Grains 97*, R. P. Behringer and J. T. Jenkins, eds., p. 483 (Balkema, Rotterdam, 1997).
29. G. H. Ristow and M. Nakagawa, "Shape Dynamics of Segregation Front in Rotating Cylinders," submitted to *Phys. Rev. Lett.*, 1998.
30. R. Hogg, D. S. Cahn, T. W. Healy, and D. W. Fuerstenau, "Diffusion Mixing in an Ideal System," *Chem. Engineering Science* **21**, 1025 (1966).
31. D. S. Cahn and D. W. Fuerstenau, "Simulation of Diffusion Mixing of Particulate Solids by Monte Carlo Techniques," *Powder Technol.* **1**, 174 (1967).
32. J. Crank, *The Mathematics of Diffusion* (Oxford University Press, London, 1975).
33. K. Wieghardt, *Theoretische Strömungslehre* (Teubner, Stuttgart, 1974).
34. O. Zik and J. Stavans, "Self-Diffusion in Granular Flows," *Europhys. Lett.* **16**, 255 (1991).